RSC Advances

ROYAL SOCIETY OF CHEMISTRY

www.rsc.org/advances

Cite this: DOI: 10.1039/c0xx00000x

www.rsc.org/xxxxxx

ARTICLE TYPE

4d Transition-metal Doped Hematite for Enhancing Photoelectrochemical Activity: Theoretical Prediction and Experimental Confirmation

Haijun Pan,[a,b] Xiangying Meng,[a,b] Jiajia Cai,[a] Song Li,[a] and Gaowu Qin[a]*

Received (in XXX, XXX) Xth XXXXXXXXX 20XX, Accepted Xth XXXXXXXXX 20XX
DOI: 10.1039/b000000x

To explore the photoelectrochemical efficiency of the hematite as a photoanode, we comprehensively investigate the electronic structures of hematite doped with 4*d* transition–metal X (X = Y, Zr, Mo, Tc, Rh, and Ru) based on the density–functional theory (DFT). The results indicate that the bandgap of hematite can be reduced by doping with the transition metal atoms, which leads to the enhanced absorption coefficient of long-wavelength photons in the visible light region. In addition, the carrier concentration can be improved by Zr, Mo, Tc, and Ru dopants. More interesting, the incorporation of Ru can also modify the conduction band edge and hence reduce the effective electron mass, leading to better electron mobility. Subsequent experiments confirm that photoelectrochemical (PEC) activity of Ru doped hematite film can be significantly improved. For example, the highest photocurrent density value of 9 at.% Ru doped hematite is 4.7 times that of undoped one at E = 1.23 V. Based on both calculations and experiments, the enhanced PEC acitivities of Ru doped hematite are derived from the improved electrical conductivity and increased visible light absorption coefficient.

Introduction

Since the discovery of Fujishima-Honda effect,[1] semiconductors have been investigated as photocatalyst materials for the technological solution to energy shortage by means of splitting water into hydrogen and oxygen. Hematite (α–Fe_2O_3) has been regarded as a potential available photocatalytic material in recent years, due to its low cost, nontoxicity, desired band gap (~2.1 eV which can capture roughly 40% of the incident solar spectrum) and photocatalytic stability in most electrolytes at pH > 3,[2–4] and has been paid increasing attention in the past few years.

However, hematite suffers from low conductivity(<1 $cm^2 V^{-1} s^{-1}$),[5] small optical absorption coefficient (~ 0.12 μm^{-1} at λ = 550 nm) ,[6–7] and fast electron–hole recombination rates(~10 ps),[8] which lead to its solar–to–hydrogen efficiency not reaching the theoretically predicted level of 16%.[10] Also, the conduction band minimum (CBM) of hematite is more negative than the requirement of hydrogen production level, thus hydrogen split by water cannot be spontaneously obtained.[11–12]

It has been experimentally reported that transition metals dopants, such as Zn, Mo, Cr, Zr, Co, Ni, Rh and Ti, play significant roles in improving PEC activities of hematite.[13–20] For example, Ti doped hematite enhances the plateau photocurrent to 3.76 mA/cm^2 due to the increase of donor density, and reduction of electron–hole recombination.[14] Zr doped hematite has been reported to show higher photocurrent density than that of undoped hematite.[17] Except for the enhancement of photocurrent density, modified hematite by doping Co or Ni gives the most thermodynamically favored reaction pathway.[18] In addition, Rh substituted $Fe_{2-x}Rh_xO_3$ can narrow the band gap, and absorb more incident solar light.[19] Thus, the photocurrent can be strongly enhanced over the wavelength of 340–850 nm at x=0.2 in the case of $Fe_{2-x}Rh_xO_3$.

First-principles have long been considered to be the effective method to explore the mechanism of experimental phenomena.[21,22] Previous experiments have reported the positive influence on the photoelectrochemical activity of Fe_2O_3 by incorporating 4*d* transition metals, such as Zr, Mo, and Rh.[17,19,20] However, the microscopic insight into the effect of 4d transition metals doping on the photocatalytic activity of Fe_2O_3 has not been gained. In this work, we systematically studied the modification of electronic properties of 4d transition metals (Y, Zr, Mo, Tc, Ru, and Rh) doped hematite based on first-principles calculations as previous reports.[23,24] Our calculation results show that donor levels can be introduced in the bandgap in Zr, Mo, Tc and Ru doped systems. Thus, electrons in donor levels can be excited into the conduction band by photons with energy samller than the bandgap. Together with the elevation of the Fermi level, carrier concentration will be enhaced in doped systems. Besides, the absorption coefficient of transition metal doped hematite increases in the visible light range due to the reduction of the bandgap. More interesting, the incorporation of Ru can modify

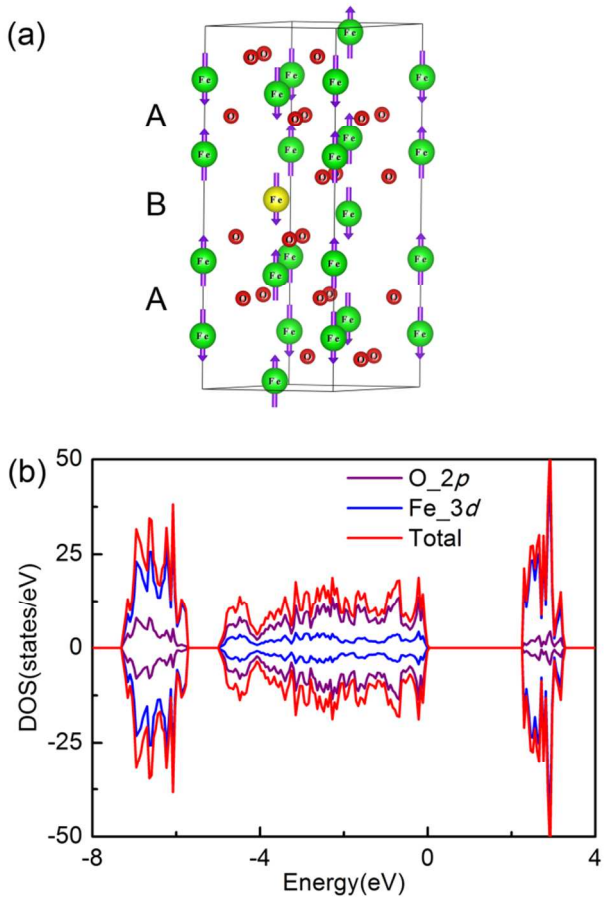

Fig. 1 (a) The hexagonal unit cell of hematite. Iron and oxygen atoms are marked by the chemical element symbols Fe and O, respectively. The directions of magnetic moment around each iron atom are represented by the arrows. The Fe atom labeled by yellow color is substituted by 4d transition metals in doping model. (b) The PDOS of pure hematite, calculated within GGA+U. The Fermi level is set to zero.

the conduction band edge and also reduce the effective mass of electrons. Our subsequent experiments confirm that the photocurrent density of Ru doped hematite is higher than the undoped one, which is well consistent with theoretical prediction.

Methods

Computational methods

The hexagonal unit cell of hematite, as is shown in Fig. 1a, has been chosen to build doping model in previous and present works.[22, 25] The experiments show that the hematite posses a stable antiferromagnetic (AFM) ground state below -10℃, in which the magnetic moment directions of iron are along the [0001].[26] There are two kinds of pairs of Fe atoms along the hexagonal [0001] axis, which are denoted by a short Fe–Fe distance (type A) and by a larger distance (type B). Iron atoms in type B have the same magnetic moment direction, whereas have the opposite direction in type A. To obtain doped hematite, we substitute one of Fe atoms with a 4*d* transition–metal atom in the hexagonal cell (shown in Fig. 1a), which is indicated by yellow sphere.[22, 25] The final dopant concentration is 8.3 at.%.

It is reported that the magnetic momentum of Fe atom originates from the difference between the charge density of spin up and spin down electrons in the *d* orbitals, which has a significant effect on electronic propertyies.[25,27] Spin-polarized calculation within the framework of density-functional theory (DFT) is an effective method to deal with the unpaired electons in solid state materials, which gives not only the quantitative theoretical determination of magnetic moment, but can also be used to explore the fundenmental mechanisms. In this study, all spin-polarized simulations are performed with the Vienna ab initio simulation package (VASP).[28] The pseudopotentials and wave functions were generated within the projector–augmented wave method.[29] The electronic wave functions were expanded in a plane–wave basis set, and a kinetic–energy cutoff of 550 eV was adopted. For exchange correlation functional, the generalized gradient approximation of Perdew, Burk and Emzerhof was employed,[30] which was widely used in the previous research of Fe_2O_3, and gave satisfactory results.[21,22,31] The Brillouin–zone integration was performed using Monkhorst–Pack grids of 11×11×10.[32] The structure was relaxed until the force is lower than 1meV/Å per atom. The framework of GG+U Invented by Dudarev et al. was selected in this simulation,[33] and the value of U-J was set to 4.3ev.[31]

The prediction of optical absorption coefficient helps us to understand optical photons interacting with the electrons in the pure and doped hematite, which can be described in terms of time–dependent perturbations of the ground–state electronic states. Electron direct transitions between occupied and unoccupied states by absorbing photons are described as a joint density of states between valence and conduction band. The imaginary part $\varepsilon^{(2)}(\omega)$ of the complex dielectric function is determined by a summation over empty states using the equation:[34]

$$\varepsilon^{(2)}_{\alpha\beta}(\omega) = \frac{4\pi^2 e^2}{\Omega} \lim_{q\to 0} \frac{1}{q^2} \sum_{c,\upsilon,k} 2\omega_k \, \delta(\varepsilon_{ck} - \varepsilon_{\upsilon k} - \omega) \times < u_{ck+e_\alpha q} | u_{\upsilon k} > < u_{ck+e_\beta q} | u_{\upsilon k} >^* \quad (1)$$

Where the indices c and υ refer to conduction and valence band states respectively, and u_{ck} is the cell periodic part of the wave functions at the k–point **k**. The real part of the dielectric tensor $\varepsilon^{(1)}(\omega)$ is obtained by the usual Kramers-Kronig transformation

$$\varepsilon^{(1)}_{\alpha\beta}(\omega) = 1 + \frac{2}{\pi} P \int_0^\infty \frac{\varepsilon^{(2)}_{\alpha\beta}(\omega')\omega'}{\omega'^2 - \omega^2 + i\eta} d\omega' \quad (2)$$

where P denotes the principle value. In this calculation, only the direct transition with the same **k** is included. The optical absorption coefficient is derived from the real and imaginary parts of the dielectric function.

Experimental methods

The Fe–Ru alloy films were deposited on conductive fluorine–doped tin oxide (FTO) glass substrate by direct current (DC) magnetron sputtering technique. The concentration of doping element (Ru/(Ru+Fe)) is defined as Ru at.%, and the mole ratio is tuned by the relative areas of the pasted chips.[35] Prior to sputtering deposition, FTO substrates were sonically cleaned using acetone, ethanol and de-ionized water each for 10 min in that sequence. Doped hematite films were obtained by placing the sputtered Fe–Ru alloy films in a tube furnace at 500

°C in air for a period of 5 h.

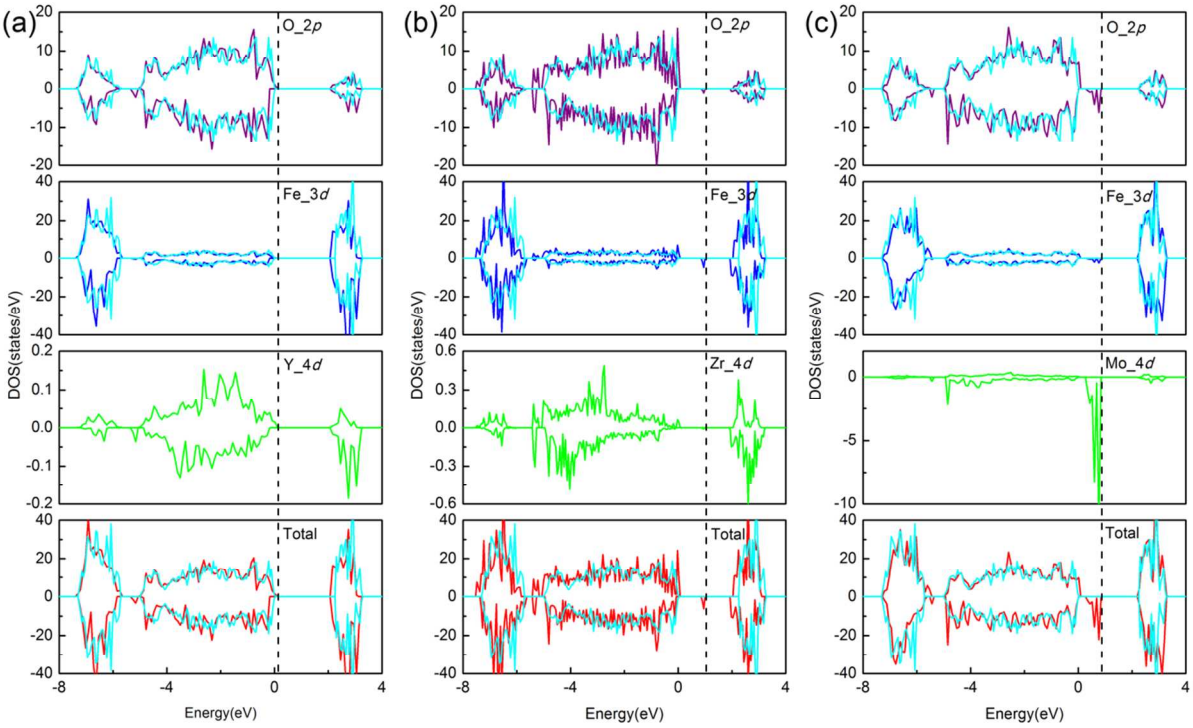

Fig.2 The PDOS of hematite doped with (a).Y, (b). Zr, and (c). Mo. For comparation, PDOSs and total DOS of hematite are plotted in each figure, which are represented by cyan. The Fermi level of pure hematite is set to zero, and the dashed line represents the Fermi level of doped hematite.

The X–ray diffraction (XRD) patterns of the samples were taken on PANnalytical–X' Pert with a Cu K_α radiation. UV–Vis spectroscopy was conducted on a Lambda 750S UV/Vis spectrometer with an integrating sphere detector, using a bare FTO substrate as reference for samples deposited on FTO.

The PEC property of each sample was tested using a 3–electrode electrochemical cell with an Ag/AgCl reference electrode and Pt plate (1 cm× 1cm) counter electrode. The working electrode (the photoanode consisting of the α–Fe_2O_3 film) with illuminated area 1.00 cm^2 was immersed in 1 M NaOH (deaerating with a nitrogen flow for 0.5 h to decrease oxygen reduction at the counter electrode). The photoelectrochemical tests of all the samples were conducted under illumination from a 300W xenon lamp (Perfect Light, PLS–SXE300) with an UV filter (Schott, KG3), which can get rid of photons with wavelength smaller than 380nm.

Results And Discussion

DFT calculation results

In Fig. 1b, the calculated band gap shows that pure Fe_2O_3 is a semiconductor with a narrow band gap of 2.30 eV. The CBM is mainly dominated by the empty Fe 3*d* states, and the valence band maximum (VBM) composed with Fe 3d and O 2*p* orbital, with O 2*p* electrons displaying a dominant role.[36] The relaxed lattice parameters for pure hematite are a=b=5.07Å and c=13.88Å .The calculated magnetic moment around iron atoms is 4.15μ_B. Thus, the electronic structure, structural parameter, and magnetic moments are all in agreement with the experimental results, which is shown in Table Ⅰ.

Table1.The structural parameter, bandgap, and magnetic momentum obtained by experiment and theoretical simulation

	a=*b*(Å)	*c*(Å)	E_g(eV)	μ_B
Expt.	5.029[37]	13.730[37]	2.1-2.3[11,38,39]	4.6-4.9[26,40,41]
Calc.	5.098[31]	13.915[31]	2.1[31]	4.2[31]
This work	5.07	13.88	2.3	4.15

The photocatalytic activity of a semiconductor is closely related to its energy band–edge structure, which determines the absorption of incident photons, the generation of electron–hole pairs, the migration of carriers, and the redox capability of excited–state electrons and holes. Given optical absorption, narrow bandgap semiconductors are more likely to exhibit high optical absorption capability and hence prone to efficiently harvest low energy photons. Beside, intermediate band level can aid low energy photons exciting electrons from VBM to CBM. The probability of generated electron–hole pairs inside the semiconductor moving to the surface is also determined by the electron conductivity σ, which can be express as follows:

$$\sigma = \frac{ne^2\tau(E_F)}{m^*} \quad (3)$$

In the formula, n represents the electron carrier concentration, and is proportional to the following equation:

$$n \propto \exp(-\frac{E_c - E_F}{k_0 T}) \quad (4)$$

If the distance between the conduction band (E_c) and Fermi level

(E_F) decreases, the electron carrier concentration will increase in the doped system. The other parameter m^* is the effective electron mass, and defined as

$$m^*(k) = (\frac{h}{2\pi})^2[\frac{\partial^2 E(k)}{\partial k^2}]^{-1} \quad (5)$$

The electron conductivity σ will be improved with the increase of the electron carrier concentration or decrease of the effective electron mass. Therefore, electronic structure analysis is fundamental for designing and fabricating semiconductor photocatalysts, and we will discuss in detail the above–mentioned electronic properties of 4*d* transition metal–doped hematite, respectively, based on electronic bonding and transition analysis. Dopant Y ($4d^15s^2$) will lose all of its three outer valence electrons to the O–2*p* orbital, which results in a close shell electronic configuration. Fig. 2a shows the project density of states (PDOS) of Y doped hematite. The valence band edge rise toward high energy level after doping with Y, hence the band gap shrinks from 2.30 eV to 2.14 eV. Except for band gap reduction, there is almost no change in the characteristic of electronic structure around Fermi level. The red shift in the band gap transition may be a main reason, leading to a better PEC performance.

Zr ($4d^25s^2$) has the similar valence electron configuration as the extensively studied dopant Ti ($3d^24s^2$). The Ti^{4+} ionic state for the Ti doping hematite is confirmed by the XPS and first principles.[15, 22] The cause of Zr^{4+} state is the same as the formation mechanism of Ti^{4+} state.Two *s* electrons and one *d* electron are accommodated by the O–2*p* orbital. The remaining 4*d* electron is higher in energy than the energy center of Fe–3*d* orbital, and flow to the nearby Fe atom, converting the Fe^{3+} to Fe^{2+}. In Fig. 2b, it can be seen that the non bonding Zr 4d electrons reside in the Fe-3d states, which appear in the middle of the band gap as a filled state under Fermi level. The emergence of foreign electron in Fe 3d orbital significantly alerts the electronic structure of occupied (-8ev ~ -6ev) and unoccupied Fe 3d states (conduction band). Finally, the unoccupied states shift towards the valence band, leading to the substantial reduction of the bandgap. Due to the narrowed bandgap of 1.95 eV, more photons in the solar spectrum can be absorbed. Second, through the intermediate level in the band gap, electrons in the valence band edge can be excited by the low energy photons to the conduction band edge. Thus, the

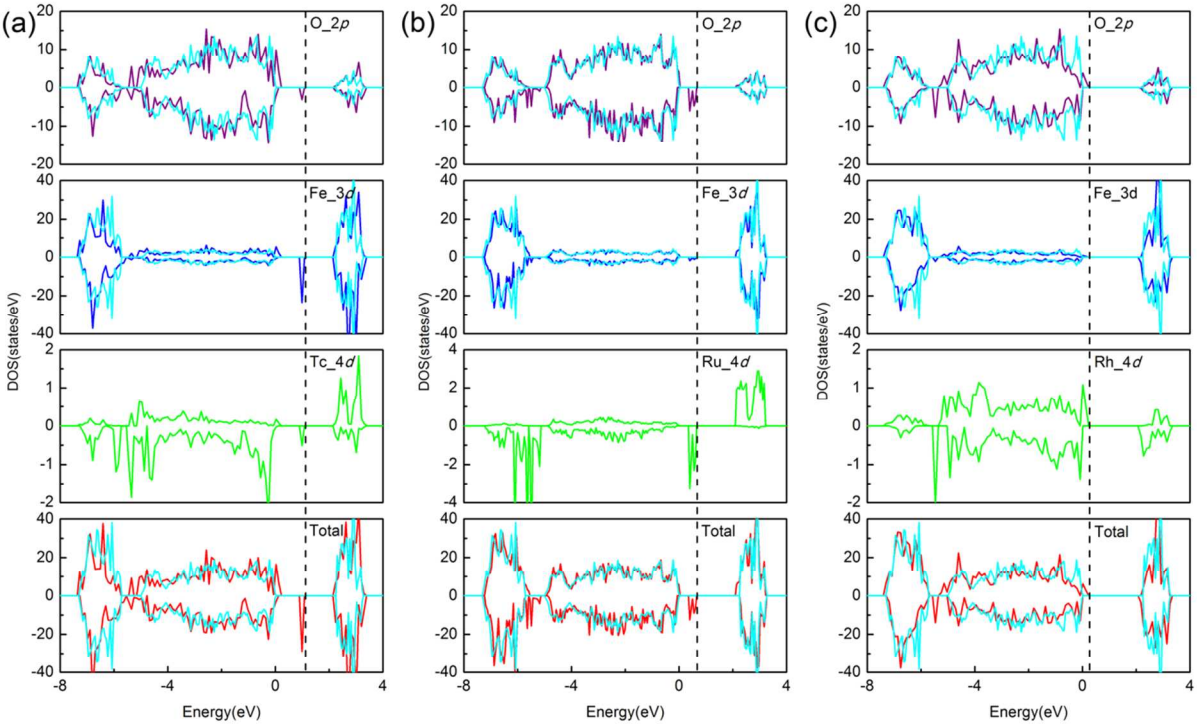

Fig. 3 The PDOS of hematite doped with (a).Tc, (b). Ru, and (c). Rh. For comparation, PDOSs and total DOS of hematite are plotted in each figure, which are represented by cyan. The Fermi level of pure hematite is set to zero, and the dashed line represents the Fermi level of doped hematite.

incorporation of Zr into Fe_2O_3 is expected to generate more electron–hole pairs than the pure hematite. In addition, the narrower gap (1.00eV) between the Fermi level and the CBM also contribute to the enhancement of the carrier concentration. In a word, the enhancement of carrier concentration is a primary reason leading to a better photocatalytic performance, which is confirmed by the experiments.[17]

Mo ($4d^55s^1$) donates one *s* electron and two of the *d* electrons to O–2*p* orbital. The Mo–4*d*–orbitals split into two sets due to the crystal field distortion, namely, the low energy t_{2g} set (including d_{xy} , d_{xz} and d_{yz} orbitals denoted as t_{2g}) and high energy e_g set (including d_z^2 and $d_{x^2-y^2}$ orbitals).[42-44] In Fig. 2c, three spin down states of t_{2g} are statured by the remaining three spin down electrons just above the top of the O–2*p* complex, and the unoccupied e_g states fall in the high energy interval. Compared to the case of Zr doping, the electrons in the impurity level is harder to transit to the conduction band edge due to a wider gap (1.47eV) between the Fermi level and the CBM, inducing a

relative lower carrier concentration . Mo doping is thus expected to be capable of achieving higher photocurrent as a positive electrode, as experiments proved. [20]

Tc ($4d^5 5s^2$) donates two *s* electrons and one of the *d* electrons to O–2*p* orbital. As is shown in Fig. 3a, the t_{2g} states are statured by three spin down electrons under the top of the valence band edge, and the other *d* electron is accepted by the vicinal Fe atom and fall in the band gap. This electronic structure is very similar to the case of Zr doping, with a larger bandgap of 2.02eV. There are no experimental reports yet for Tc doping, but it may be a promising candidate as a photoanode.

Ru ($4d^7 5s^1$) is likely to lost one *s* electron and two of the *d* electrons to the surrounding O, leading to chemically a stable half filled 4*d* orbital. The t_{2g} states are statured by three spin down electrons, and located in the energy range of -8～-6 eV. The occupied e_g states fall in the band gap, just above the valence band edge. The band gap slightly shrinks 0.15eV compare with the pure hematite. More significantly, the Ru 4*d* states are positioned at the conduction band edge (in Fig. 3b). This means the heavy effective electron mass of pure hematite can be effectively lighten due to the modification of conduction band edge by the Ru 4*d* states. Therefore, it would improve the electron mobility in the Ru doped hematite.

Rh ($4d^8 5s^1$) is prone to form semiconductor compound Rh_2O_3, which has a corundum structure. In Rh_2O_3, Rh in Rh^{3+} ionic state releases all its six electrons into the t_{2g} states, forming a fake with close shell electronic configuration. Rh replaces a Fe atom in the Fe_2O_3, and reproduces the ionic state and the bonding mechanism in the Rh_2O_3. In Fig. 3c, we can see that the t_{2g} state deep under the valence band edge located in the energy range of -4 eV to -6 eV, and the unoccupied states are separated to the high energy position above the conduction band edge. This isovalent doping brings a band gap reduction, about 0.26 eV smaller than the pure hematite, and thus enhancing the photon absorption. The recently reported experimental result confirmed the constantly band gap reduction in the $Fe_{2-x}Rh_xO_3$ ($0.0 \le x \le 2.0$) with the increasing ingredient *x*, which well supported our prediction. [19]

Table. Ⅱ Computational structural parameters of oxygen octahedron surrounding the dopant X (X = Y, Zr, Mo, Tc, Rh, and Ru), band gap values, and distances between E_F and CMB.

	Bond length(Å) (X-O)		Bond angle (O-X-O)		Band gap(eV)	E_c-E_F
Pure hematite	1.967	2.119	78.712	101.94	2.30	2.30
Y	2.231	2.382	71.558	110.676	2.14	2.14
Zr	2.130	2.169	83.002	99.861	1.95	1.00
Mo	2.097	2.153	80.454	100.444	2.26	1.47
Tc	2.047	2.403	80.872	98.788	2.02	1.03
Ru	2.078	2.272	75.096	105.218	2.15	1.47
Rh	2.071	2.073	82.654	97.925	2.04	2.04

We find that the incorporation of 4*d* transition metals leads to significant distortion of octahedron, which leads to a crystal field splitting. Here, we list the structure parameters between the transition metals and the surrounding O atoms in Table Ⅱ. Through the two kinds of bond angles for O–X–O and bond length, it can be inferred that the distortion of octahedron comply with the following order: Y>Zr>Mo>Tc>Rh>Ru. Among these transition metals, the chemical environment for Ru atom is similar to the substituted Fe atom, which leads the unoccupied Ru 4d orbital to modify the effective electron mass and hence to improve the photocurrent density.

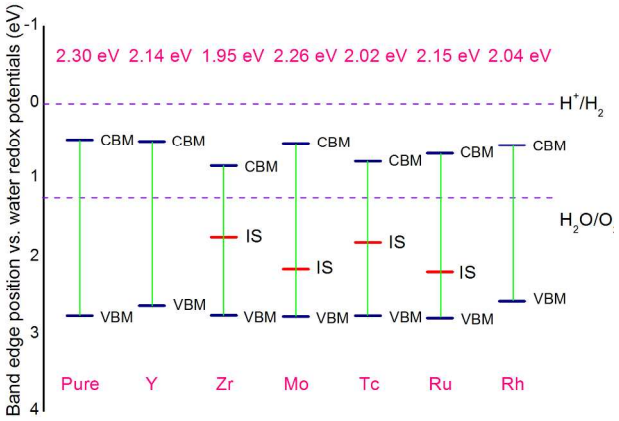

Fig. 4 Computed band edge positions of pure and doped hematite (solid blue lines) with respect to the redox potential of water splitting at pH = 2 (dashed violet lines). The solid red lines represent the intermediate states in the band gap.

The proper band edge position is one of requirements for ideal photocatalyst, ie, VBM is below the water oxidation level, and CBM locats above the hydrogen production level. It is reported that Fe_2O_3 can not split water spontaneously, due to the improper CBM. In order to investigate whether dopants could improve the conduction band edge position, we calculate the variation of VBM and CBM of doped hematite (shown in Fig. 4). For pure hematite, the band edge positions with respect to the normal hydrogen electrode (NHE) potential are obtained from the experimental values,[11] which is often used in previous literature.[23,45,46] For 4*d*–transiton metal doped hematite, the O 1*s* core level is adjusted to the same energy level with the pure one, and then the relative shift of VBM and CBM is calculated to obtain the correct alignment.[47] Compared to the pure hematite, the Fe–isovalent dopants (Y, Rh) can obviously promote the VBM toward a higher energy, which mainly cause by the orbital hybridization between O 2*p* and dopant 4*d* orbitals, while leaving the CBM almost unchanged. On the contrary, doping of Zr and Tc makes the CBM obviously leave away from the reduction potential level. For another case, redox potential for Mo and Ru doped hematite remained almost unchanged. In summary, there is no effective doping to shift the CBM of hematite toward hydrogen production level, which indicates that the spontaneous production of hydrogen for 4*d* transition–metal doped hematite is still not realized.

The optical absorption coefficient is theoretically calculated in order to further clarify the band structure of pure and doped Fe_2O_3, as shown in Fig. 5. The theoretical absorption peaks of pure hematite locate in the visible light region (450 nm) and the UV light region (340 nm), respectively, which agrees well with the reported DFT result.[48, 49] However, there is a discrepancy with experimental absorption peaks, namely, the Laporte–forbidden *d*–d indirect transition (540nm) and the direct ligand–to–metal charge–transfer (LMCT) transitions (400nm), respectively.[7] This difference may originate from reason as follows: on the one hand,

the excited–state effects are not considered in the DFT

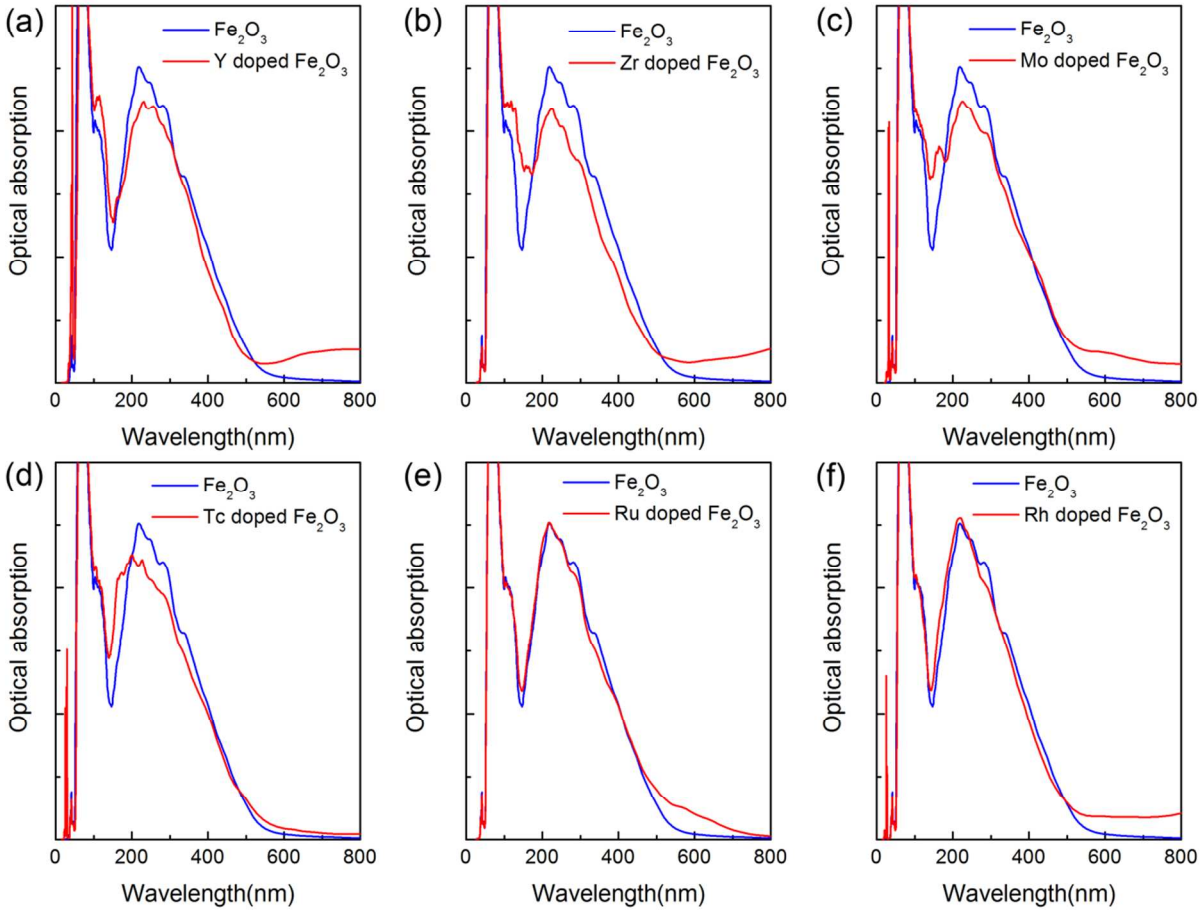

Fig. 5 Optical absorption spectra of α-Fe_2O_3 doped with (a). Y, (b). Zr, (c). Mo, (d). Tc, (e). Ru, and (f). Rh, respectively.

calculations; On the other hand, the absorption coefficient isclosely related to the shape and size of the sample, the surface morphology, and inherent defects in the thin film.[50-52] It is hard to match experimental and theoretical observables, and we mainly fuscous on the trend of absorption coefficient after transition metal doping. Among these dopants, the optical absorption coefficient of Tc doped hematite does not improve significantly. Except for Tc, the absorption region of 4*d*–transiotn metal doped hematite is become wider in the visible region. Moreover, the ability to absorb photons is especially enhanced for Mo and Ru doping over the entire visible region due to the narrowed band gap and the existence of widely distributed impurity states in the band gap. Therefore, more excited electron-hole pairs would be expected in Ru and Mo doped hematite due to the strong absorption of photons in the visible light range, which especially contribute to the efficiency of PEC water splitting.

Until now, the PEC efficiency of Zr, Mo and Rh doped hematite have been experimentally confirmed. [17, 19, 20] The enhancement in the photocurrent is attributed to the improved conductivity induced by doping with Zr and Mo atom, respectively. With regard to Rh, this enhancement is accompanied with the increased absorption coefficient over a wavelength range of 340–850 nm. For the three kinds of dopants, the calculated results show that the positive effect is related to either the carrier concentration or the reduction of the bandgap. However, for Ru doped hematite, besides the modified carrier concentration and absorption coefficient, the reduced electron effective mass is predicted to be a key factor toward the enhancement of the PEC efficiency. Since the distinct feathers of the electronic structure, we pay special attention to Ru doped hematite, and conduct the subsequent experiments.

Experimental results

In order to further clarify the validity of our theoretical predictions, Ru doping experiment was performed in this work. Fig. 6 shows scanning electron microscope (SEM) images of the undoped and Ru–doped Fe_2O_3 thin films prepared by magnetron sputtering deposition method. For pure hematite thin film, it can be seen that the surface is covered by uniform and condensed rod–like grains. Compared with the pure samples, the morphology of the modified hematite samples almost remain unchanged, except for a slight decrease in the grain size.

Fig. 7a shows X–ray diffraction (XRD) patterns of undoped and Ru–doped hematite deposited on FTO substrate. It can be seen that there is no XRD peaks corresponding to impurity phase in Ru doped samples, and these data confirm the successful

preparation of the Ru doped hematite phase. As shown in Fig. 5e, the theoretical absorption curve in the UV-light region of hematite is not significantly affected by Ru dopant. Consequently, the effects of the UV-light is not included in the experimental work. Fig. 7b presents the experimental measured optical absorption spectra of the undoped and Ru doped hematite samples. It shows that incorporating Ru significantly enhances the absorbance of hematite for wavelengths in the visible light band for all samples.

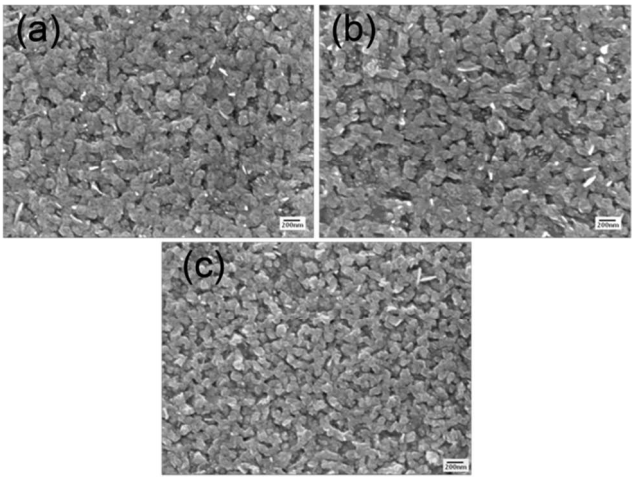

Fig. 6 SEM images of prepated samples (a) Fe_2O_3, (b) 6 at.% and (c) 9 at.% Ru doped Fe_2O_3. The scale bar in the insets is equal to 200 nm.

Photocurrent–voltage characteristic curves of doped hematite were measured in 1.0 M NaOH solution, using a three electrode setup with Ag/AgCl as reference electrode. From the J–V curves shown in Fig. 7c, it is quite clear that the doping of Ru in α–Fe_2O_3 at various levels improved the PEC response. Compared to the pure hematite film (only 0.031 mA/cm^2 at 1.23 V), the photocurrent density can increase up to 0.121 mA/cm^2 for 6 at.% and 0.148 mA/cm^2 for 9 at.% Ru doped hematite, respectively. In the case of higher voltage bias, the photocurrent density of Ru doped hematite drastically increases with Ru doped concentration. For example, the photocurrent density of pure hematite is 0.091 mA/cm^2 at 1.40 V, and that of Ru doped one can reach 0.277 mA/cm^2 and 0.41 mA/cm^2 for the 6 at.% and 9% Ru doping, respectively. Samples of Ru doped hematite show intense photocurrent density with the increase of bias voltage, and 9 at.% Ru doped hematite film exhibits much higher PEC activity, especially at a higher voltage bias.

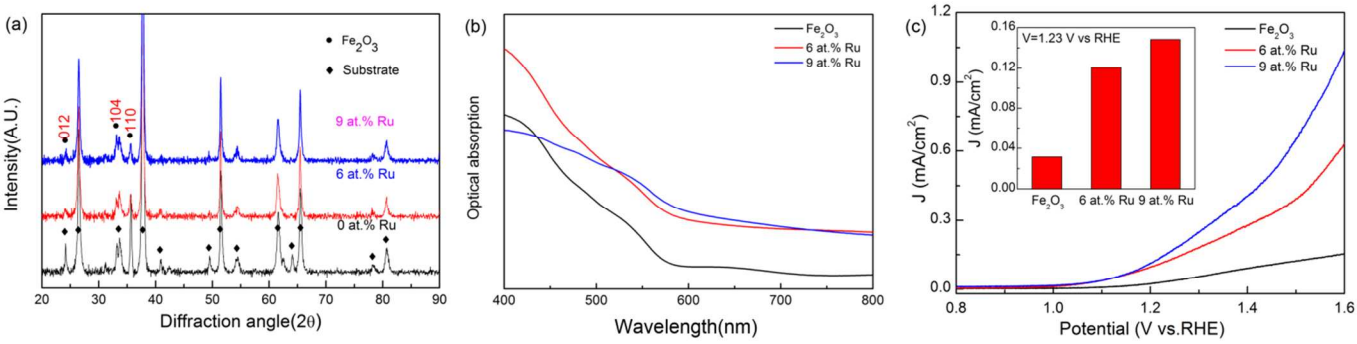

Fig.7 (a) The XRD pattern of undoped α-Fe_2O_3 and Ru doped α-Fe_2O_3 after annealed at 500 °C in air for a period of 5h (b) Absorbance spectra of undoped α-Fe_2O_3 and Ru doped α-Fe_2O_3.(c) J-V scans collected for undoped and Ru doped hematite films, with a scan rate of 20 mV/s.

Disscussion

Taking into account the highest power density of the visible light region in solar energy, it is important to realize the excellent light absorption property to achieve high quantum efficiency. Due to the narrowed bandgap and the emergence of the impurity states in the bandgap, the adjusted band structure of Ru doped hematite is helpful to the electronic transition from VBM to CBM through absorption of photons in the visible region. As shown in Fig. 5e, the theoretically calculated optical absorption coefficient of Ru doped hematite is significantly enhanced within the visible light rang of 410~800nm, which has the similar trend as experimental results shown in Fig. 7b. However, experimentally observed results deviate from theoretical result at some points. Unlike the calculated absorption coefficient, the experimental observed data does not intend to superpose with the original curve at 800nm. In the region of wavelength less than 410nm, the 6% at. Ru doped hematite still has a higher the absorbtion coefficient than the pure hematite. Even the absorption coefficient is not consistent with each other in these two doped hematites around wavlength of 400nm. Through the comparation, it can be indicated that this difference may come from the continually variable surface topography and the doped grains in the experiment. In oreder to exclude the uncertainty in the experiment, it is rational to analyze the enhanced absorbtion coefficient by the calculated results.The enhancement in the visible region (410nm~580nm) may originate from the intra–band transition between the Fe 3*d* and the Ru 3*d*, as well as the reduced bandgap. The ability to absorb photons with wavelength of 580–800 nm can be attributed to the intermediate states. The electron in the valence band can be excited to the intermediate states by the low–energy photons, and then excited once again by low–energy photons to eventually reach the conduction band.[53] It can be inferred that the enhanced visible light absorption for Ru doped hematite is one of the intrinsic factors contributing to the improved PEC activity in our experiment.

In the previous work, Cheng et al. indicate that a high ratio of surface recombination has a greater influence on the carriers with low energy, and leads to a sharp decrease of the incident photon–to–electron conversion efficiency in the visible light region.[54] From the computational results, it is observed that the heavy effective electron mass of pure hematite can be lightened due to

the modification of conduction band edge by the Ru 4*d* states. Thus, we calculate the E–k diagram around the CBM within the first Brillouin zone along the specific high symmetry directions, and obtain the effective electron mass with the expression:

$$m^*(k) = (\frac{h}{2\pi})^2[\frac{\partial^2 E(k)}{\partial k^2}]^{-1}$$

In hematite，the conductivity is anisotropic. For example, the conductivity in (0001) plane is four orders of magnitude higher than that in directions perpendicular to (0001) plane.[55] Therefore, Therefore, it is meaningful to understand the movement of electrons in (0001) plane. The calculated effective electron mass of Ru doped hematite is 5.15 m_0 along [10-10] direction, and 2.94 m_0 along [11-20] direction, respectively, where the m_0 is represent for mass of a free electron (9.11×10^{-31}kg). They are smaller than 5.51 m_0 and 3.02 m_0 of undoped hematite in the corresponding directions. With smaller effective electron mass and higher carrier concentration, the conductivity in the film can be enhanced, which could make more electron–hole pairs migrate to the surface to involve in the redox reaction. This can also be viewed as a key factor, leading to the better PEC performance of Ru–doped hematite thin films.

The performances of transition metal doped hematite photoelectrode are widely investigated and demonstrate positive effect at some distance. However, it is difficult to discern the intrinsic cause of the improvement, due to the various factors in experiment, such as preparation method, doping concentration, the surface morphology, thin film thickness, and annealing temperature. [14-16, 40] Thus, the fundamental electronic structure of doped bulk hematite is calculated using DFT simulation to confirm the favorable effective electronic mass, carrier concentration, and electron transition in this study. Though the PEC performance of Ru doped α–Fe_2O_3 was not as excellent as previous reported results by the other dopants, [15,16] the Ru dopant may display a good performance in an optimized experiment in the near future.

Conclusions

In summary, we have investigated the electronic structure and optical absorption coefficient of 4*d* transition metal doped hematite based on the density functional theory. Our calculation results show that the PEC activity of hematite doped by Y, Zr, or Mo can be improved, which is well consistent with previous experimental results. More interestingly, we theoretically predict that the Ru doped hematite is a preferable candidate for PEC hydrogen production through water splitting, based on the following two facts. First, the conductivity can be improved by the reduced effective electron mass together with an improved carrier concentration. Second, the incorporation of Ru can enhance the optical absorption coefficient in the visible light region, which may lead to more electron-hole pairs in doped hematite. The further experiments well confirm our prediction in the case of Ru doping, involving both light absorption and PEC activity. The mutually consistent results in both calculation and experiments are not only helpful to understand the mechanism of modified electronic properties of hematite doped by 4*d* transition metals, but also of value in further developing modified hematite with higher photocatalytic activity by proper element doping.

Acknowledgments

The authors gratefully acknowledge financial support by National Natural Science Foundation (No. 51001025 and No. 51002026), the Fundamental Research Funds for the Central Universities (No.130405003, No.11080001), Program for Changjiang Scholars and Innovative Research Team in University (No. IRT0713) and National High Technology Research and Development Program of China (Grant No. 2013AA031601).

Notes and references

[a] *Key Laboratory for Anisotropy and Texture of Materials (Ministry of Education), Northeastern University, Shenyang 110819, People's Republic of China*
[b] *College of Sciences, Northeastern University, Shenyang 110819, People's Republic of China*
**Corresponding author. E-mail: qingw@smm.neu.edu.cn*

1 A. Fujishima, K. Honda, Nature 1972, 238, 37.
2 P. Merchant, R. Collins, R. Kershaw, K. Dwight, A. Wold, J. Solid State Chem. 1979, 27 (3), 307.
3 K. Sivula, F. Le. Formal, M. Grätzel, ChemSusChem, 2011, 4, 432.
4 T. Lindgren, L. Vayssieres, H. Wang, S. E. Lindquist, Chem. Phys. Nanostruct. Semicond. 2003, 83.
5 K. M. Rosso, D. M. A. Smith, M. J. Dupuis, Chem. Phys. 2003, 118, 6455.
6 I. Cesar, K. Sivula, A. Kay, R. Zboril, M. Grätzel, J. Phys. Chem. C ,2009, 113, 772.
7 J. S. Jang, J. Lee, H. Ye, F. R. F. Fan, A. J. Bard, J. Phys. Chem. C, 2009, 113, 6719.
8 N. J. Cherepy, D. B. Liston, J. A. Lovejoy, H. M. Deng, J. Z. Zhang, J. Phys. Chem. B, 1998,102 (5), 770.
9 M. P. Dare–Edwards, J. B. Goodenough, A. Hamnett, P. R. Trevellick, J. Chem. Soc. Faraday Trans. I, 1983, 79, 2027.
10 A. B. Murphy, P. R. F. Barnes, L. K. Randeniya, I. C. Plumb, I. E. Grey, M. D. Horne, J. A. Glasscock, Int. J. Hydrogen Energy 2006, 31, 1999.
11 T. Bak, J. Nowotny, M. Rekas, C. C. Sorrell, Int. J. Hydrogen Energy 2002, 27, 991.
12 M. C. Toroker, D. K. Kanan, N. Alidoust, L. Y. Issero, P. Liao, E. A. Carter, Phys. Chem. Chem. Phys., 2011, 13, 16644.
13 S. Kumari, A. P. Singh, C. Tripathi, D. Chauhan, S. Dass, R. Shrivastav, V. Gupta, K. Sreenivas, V. R. Satsangi, Int. J. Photoenergy, 2007, 87467.
14 J. Deng, J. Zhong, A. Pu, D. Zhang, M. Li, X. Sun, S. T. Lee, J. Appl. Phys., 2012, 112, 084312.
15 C. Miao, T. Shi, G. Xu, S. Ji, C.Ye, Appl. Mater. Interfaces, 2013, 5, 1310.
16 O. Zandi, B. M. Klahr, T. W. Hanmann, Energy Environ. Sci., 2013, 6, 634.
17 P. Kumar, P. Sharma, R. Shrivastav, S. Dass, V. R. Satsangi, Int. J. Hydrogen Energy, 2011, 36, 2777.
18 P. Liao, J. A. Keith, E. A. Carter, J. Am. Chem. Soc., 2012, 134, 13296.
19 M. Seki, H. Yamahara, H. Tabata, Appl. Phys. Express, 2012, 5, 115801.
20 A. Kleiman–Shwarsctein, Y. S. Hu, A. J. Forman, G. D. Stucky, E. W. McFarland, J. Phys. Chem. C, 2008, 112, 15900.
21 X. Y. Meng, G. W. Qin, S. Li, X. H. Wen, Y. P. Ren, W. L. Pei, L. Zuo, Appl. Phys. Lett., 2011, 98, 112104.
22 M. N. Huda, A. Walsh, Y. F. Yan, S. H. Wei, M. M. Al–Jassim, J. Appl. Phys., 2010, 107(12), 123712.
23 P. H. Borse, J. S. Lee, J. Appl. Phys., 2006, 100, 124915.
24 H. Yang, W. Mi, H. Bai, Y, Cheng, RSC Adv., 2012, 2, 10708.

25 J. Velev, A. Bandyopadhyay, W. H. Butler, S. Sarker, Phys. Rev. B, 2005, 71, 205208.
26 F. J. Morin, Phys. Rev., 1950, 78, 819.
27 G. Rollmann, A. Rohrbach, P. Entel, J. Hafner, Phys. Rev. B, 2004, 69, 16510,
28 G. Kresse, J. Furthmuller, Phys. Rev. B, 1996, 54, 11169.
29 G. Kresse, D. Joubert, Phys. Rev. B, 1999, 59, 1758.
30 J. Perdew, K. Burke, M. Ernzerhof, Phys. Rev. Lett., 1996, 77, 3865.
31 N. J. Mosey, P. Liao, E. A. Carter, J. Chem. Phys, 2008, 129, 014103.
32 H.J. Monkhorst, J.D. Pack, Phys. Rev. B, 1976, 13, 5188.
33 S. L. Dudarev, G. A. Botton, S. Y. Savrasov, C. J. Humphreys, A. P. Sutton, Phys. Rev. B, 1998, 57, 1505.
34 M. Gajdoš, K. Hummer, G. Kresse, J. Furthmüller, F.Bechstedt, Phys. Rev. B, 2006, 73, 045112.
35 B. Yang, G. Qin, W. Pei, S. Li, Y. Ren, S. Ishio, J. Chem. Phys, 2008, 129, 014103.
36 A. Fujimori, M. Saeki, N. Kimizuka, M. Taniguchi, S. Suga, Phys. Rev. B, 1986, 34, 7318-7328.
37 L. Pauling and S.B. Hendricks, J. Am. Chem. Soc., 1925, 47, 781.
38 J. A. Glasscock, P. R. F. Barnes, I. C. Plumb, N. Savvides, J. Phys. Chem. C, 2007, 111, 16477-16488
39 K. Sivula, F. Le. Formal, M. Grätzel, ChemSusChem, 2011, 4, 432.
40 L. W. Finger and R. M. Hazen, J. Appl. Phys., 1980, 51, 5362.
41 Y. Sato and S.-i. Akimoto,J. Appl. Phys., 1979, 50, 5285.
42 S. S. Zumdahl, Chemical Principles (5th ed.). 2005, 550–551, 957–964.
43 M. S. Silberberg, Chemistry: The Molecular Nature of Matter and Change (4th ed.), 2006, 1028–1034.
44 D. F. Shriver, P. W.Atkins, Inorganic Chemistry (4th ed.), 2001, 227–236.
45 J. Wang , T. Fang , L. Zhang, J. Feng , Z. Li , Z. Zou, Journal of Catalysis, 2014, 309, 291.
46 W. Yang, Y. Wen, R. Chen, D. Zeng, B, Shan, Phys. Chem. Chem. Phys., 2014, 16, 21349.
47 C. G. Van de walle, J.Neugebauer, J. Appl. Phys., 2004, 95, 3851.
48 C. Xia, Y. Jia, M. Tao, Q. Zhang, Phys. Lett. A, 2013, 377, 1943.
49 H. Yang, Q. Mi, H. Bai, Cheng, Y. RSC Adv., 2012, 2, 10708.
50 H. M. Fan, G. J. You, Y. Li, Z. Zheng, H. R. Tan, Z. X. Shen, S. H. Tang, Y. P. Feng, J. Phys. Chem. C, 2009,113, 9928.
51 G. T. Boyd,; Z. H. Yu,; Y. R. Shen, Phys. Rev. B, 1986, 33, 7923.
52 Y. P. He, Y. M. Miao, C. R. Li, S. Q. Wang, L. Cao, S. S. Xie, G. Z. Yang, B. S. Zou, Phys. Rev. B, 2005, 71, 125411.
53 A. Luque, A. Martí, Phys. Rev. Lett., 1997, 78, 5014.
54 W. Cheng, J. He, Z. Sun, Y. Peng, T. Yao, Q. Liu, Y. Jiang, F. Hu, Z. Xie, B. He, S. Wei, J. Phys. Chem. C, 2012, 116, 24060.
55 K. M. Rosso, D. M. A. Smith, M. Dupuis, J. Chem. Phys., 2003, 118, 6455.